# Seasonal and El Niño Variability in Weekly Satellite Evaporation over the Global Ocean During 1996-1998

Alberto M. Mestas-Nuñez, [1][*] Abderrahim Bentamy, [2]    and Kristina B. Katsaros [1]

[1]*Cooperative Institute for Marine and Atmospheric Studies, University of Miami, 4600 Rickenbacker Causeway, Miami, Florida 331499, U.S.A.*

[2]*Institut Français pour la Recherche et l'Exploitation de la MER, B.P. 70, 29280 Plouzané, France*

October 2005

---

[*] Corresponding author address:  NOAA/AOML, 4301 Rickenbacker Causeway, Miami, FL 33149.  Email: alberto.mestas@noaa.gov

**Abstract**

The seasonal and anomaly variability of satellite-derived weekly latent heat fluxes occurring over the global oceans during a 3-year period (January 1996 – December 1998) is investigated using EOF and harmonic analyses.  The seasonal cycle of latent heat flux is estimated by least square fitting the first three (annual, semi-annual and 4-month) harmonics to the data.  The spatial patterns of amplitudes of these harmonics agree well with the corresponding patterns for wind speed. The annual harmonic captures an oscillation that reflects high evaporation in late fall/early winter and low evaporation in late spring/early summer in both hemispheres, with larger amplitudes in the northern hemisphere over the western side of the oceans, and significant phase differences within each hemisphere.  The main feature of the semiannual harmonic is its large amplitude in the Asian monsoon region (e.g., in the Arabian Sea its amplitude is about 1.5 larger than the annual) and the out of phase relationship of this region with the high latitudes of the North Pacific, consistent with other studies.  The third harmonic shows three main regions with relative large amplitudes, one in the Arabian Sea and two our of phase regions in the central mid-latitude North and South Pacific. After removing this estimate of the seasonal cycle from the data, the leading EOF of the anomalies isolates the 1997-1998 El Niño signal, with enhanced evaporation in the eastern tropical Pacific, around the Maritime Continent, in the mid-latitude North and South Pacific and the equatorial Indian Ocean, and reduced evaporation elsewhere around the global ocean during April 1997 – April 1998.  This pattern is consistent with known patterns of ENSO variability and with the "atmospheric bridge" teleconnection concept.  Our study illustrates the usefulness of satellite derived latent heat fluxes for climatic applications.

## 1. Introduction

In the tropical oceans, the latent heat of evaporation to a large extent balances the large input of solar radiation. Knowing its variability, particularly over space which is larger than that of solar radiation (e.g., da Silva et al. 1994), is therefore very important for determining the net heating of the ocean which in turn determines the sea surface temperature (SST), the subsurface thermal structure, and the heat available for poleward advection by the ocean currents. In addition, evaporation also plays an important role in the fresh water budget with the net evaporation (evaporation minus precipitation) leading to changes in sea surface salinity. In the atmosphere, the presence of water vapor and its vertical movement within the troposphere are directly related to cloud formation, precipitation, and the attendant release of latent heat. Water vapor is also the most important greenhouse gas in the atmosphere and its horizontal transport (*e.g.,* from tropics to poles or from oceans to continents) constitutes the atmospheric branch of the global hydrological cycle (e.g., Peixoto and Oort 1992; Sohn et al. 2004).

Another important role of oceanic evaporation is to provide a positive thermodynamic feedback (referred to as the wind-evaporation-SST or WES feedback) mechanism for air-sea interactions in the tropics (Xie and Philander 1994). In the Pacific, the WES feedback mechanism is invoked when explaining the meridional migration of the ITCZ (Xie and Philander 1994). In the tropical Atlantic, this mechanism has been hypothesized to explain decadal changes of the inter-hemispheric SST gradient (Carton et al. 1996; Chang et al. 1997), which modulates precipitation over northeast South America (Moura and Shukla 1981) and northwest Africa (Folland et al. 1986). Understanding the role of evaporation in these tropical air-sea interactions is challenging because the heat flux anomalies involved are well below the observational limit of 10-20 W m$^{-2}$ (Carton et al. 1996).

The importance of accurately estimating latent heat flux over the global oceans is widely recognized in the global scientific community (e.g., Curry et al. 2004). Traditionally, the main sources of global latent heat flux datasets have been atmospheric analyses and reanalyses from numerical weather prediction centers such us National Centers for Environmental Prediction/National Center for Atmospheric Research (NCEP-NCAR) and the European Center for Medium-Range Weather Forecasts (ECMWF).

More recently several satellite-derived products based on passive satellite microwave measurements (SSM/I) combined with SSTs from infrared observations (AVHRR) are also available. Examples of these datasets are the Hamburg Ocean Atmosphere Parameters from Satellite Data known as HOAPS (Schulz et al. 1997), the Goddard Satellite-Based Surface Turbulent Fluxes version 2 known as GSSTF2 (Chou et al. 2003; Chou et al. 2004) and the Japanese Ocean Flux Data Sets with Use of Remote Sensing Observations  know as J-OFURO (Kubota et al. 2002; Kubota et al. 2003).

To enhance the resolution of satellite-based estimates of latent heat fluxes over the global ocean Bentamy et al. (2003) presented the methodology and quality assessment to produce a 9-month dataset that incorporated satellite scatterometer wind speeds along with SSM/I and AVHRR data.  Briefly, the turbulent latent heat flux, $H_L$, was calculated from mean near surface variables using the following bulk formula:

$$H_L = -l \, \rho \, C_E \, \overline{U}_{10_N} (q_{10_N} - q_s), \tag{1}$$

where $l$ is the coefficient for latent heat of evaporation; $\rho$ is the air density; $C_E$ is the bulk transfer coefficient for water vapor (Smith 1988; Hasse and Smith 1997); $\overline{U}_{10_N}$ is the surface wind speed at 10-m height and neutral stratification; $q_{10_N}$ is the specific humidity at 10-m height and neutral stratification; and $q_s$ is the specific humidity at the sea surface equivalent to the saturation value over a fresh water surface at the SST and including the reduction due to salt by the factor 0.98. The variables, $\overline{U}_{10_N}$, $q_{10_N}$, and SST were estimated from satellite observations.

The Bentamy et al. (2003) study concentrated on the 9-month period (October 1996 through June 1997) during which the NSCAT satellite provided data along two 500-km swaths that yielded 50-km resolution wind vectors.  Simultaneously, the ERS-2 satellite obtained a single 600-km swath of wind vectors at 50-km resolution, while several SSM/Is provided wind speeds over 1400-km swaths at 50-km resolution.  These SSM/Is also provided near surface humidity by a proxy estimate (Schulz et al. 1993; Schulz et al. 1997) and SST was obtained from the Reynolds analysis (Reynolds and Smith 1994). The resulting weekly and monthly global evaporation rate estimates were produced at the Institut Français pour la Recherche et l'Exploitation de la Mer (IFREMER) in France. These estimates compared reasonably well (rms of about 40 W m$^{-2}$) with the

Comprehensive Ocean-Atmosphere Data Set (COADS) data and with surface flux estimates from the NCEP-NCAR reanalysis and ECMWF analyses. Details of these comparisons are shown by Bentamy et al. (2003), where differences between satellite estimates and the numerical analyses and reanalyses estimates are discussed.

Recently, a 1-year version (October 1996-September 1997) of the Bentamy et al. (2003) satellite wind speed and latent heat flux estimates were used to describe the patterns of week-to-week variability in the tropical and subtropical Atlantic Ocean (Katsaros et al. 2003). The variability of latent heat flux was dominated by 3-4 week fluctuations in latent heat flux and wind speed. The most significant finding was a strong northeast trade wind burst that originated near the northwest African coast in early February 1997, persisted for five weeks as it crossed the Atlantic and dissipated in the Caribbean Sea.

In this study, we describe the spatial and temporal structure of the seasonal and anomaly variability in the weekly $1° \times 1°$ gridded latent heat flux fields of Bentamy et al. (2003). We use an updated 3-year version (January 1996 - December 1998) of their dataset, a period that includes the strong 1997-1998 El Niño and part of the weak 1998-1999 La Niña events (McPhaden 1999). We picked this time period to see if the Bentamy et al. (2003) evaporation fluxes are able to capture the ENSO signal and thus help justify their extension to a multi-year dataset. The seasonal cycle is estimated using harmonic analyses. The anomaly variability is studied by removing this seasonal cycle from the data. The results are presented in section 2 and include a description of the 3-year mean and standard deviation (section 2.*a*), a description of the seasonal variability (section 2.*b*), and an analysis of ENSO variability (section 2.*c*). Summary and concluding remarks are given in section 3.

## 2. Results

### a. Mean and standard deviation

The mean and standard deviation of the weekly latent heat fluxes over the 3-year (1996-1998) period are shown in the upper and lower panels of Fig. 1, respectively. Positive values of the latent heat fluxes represent upward ocean-to-atmosphere fluxes (i.e. oceanic cooling). Here and in the rest of the paper we have not used time series for

which there were any missing weekly estimates, as can be seen by the white oceanic regions in Fig. 1. The mean evaporation pattern (Fig. 1, upper panel) has structure qualitative similar to annual mean climatological estimates (e.g., Esbensen and Kushnir 1981; Josey et al. 1998). Our 3-year period is too short for quantitative comparisons against multi-year climatologies. However, our mean evaporation estimates are likely an overestimation of the long-term mean because the satellite wind speed estimates are generally larger than buoy observations during the period 1996-1997 (Bentamy et al. 2002).

In general, the large-scale pattern of evaporation (Fig. 1) shows low values over the colder high-latitude waters and large values over the warmer tropical and mid-latitude waters. At tropical latitudes, there are also low values in areas of upwelling, such as along the equator, over the cold tongue regions of the Pacific and Atlantic, and off the coast of northwest Africa and the California Current. At mid latitudes, large values of evaporation are seen over the Kuroshio and Gulf Stream currents and around Australia. The maximum values of evaporation are found in the Caribbean Sea ($> 200$ W m$^{-2}$).

The latent heat flux pattern in Fig. 1 (upper) compares very well with the 1992-1994 average of the J-OFURO dataset (Kubota et al. 2003, see their Fig. 1a) and with the 1992-1993 average of the GSSTF2 dataset (Chou et al. 2004, see their Fig. 7a). Even though the observational period of these studies also include an El Niño event (the 1991-1993, which was not as strong as the 1997-1988 event in our period), their mean evaporation estimates in general appear to be larger than ours. However, a detailed comparison of our satellite latent heat fluxes with these other products is beyond the scope of this paper. Compared to the NCEP-NCAR reanalysis (Kalnay et al. 1996) over the subtropics, both J-OFURO and GSSTF2 generally give larger values than NCEP-NCAR (Kubota et al. 2003; Chou et al. 2004) while our product is generally smaller (Bentamy et al. 2003).

The standard deviation of the 3-year weekly time series of evaporation (Fig.1, lower panel) shows moderate values (about 40 W m$^{-2}$) over most areas of the world ocean. The lower standard deviation values are found in the southern hemisphere south of about 40ºS, in the region of the Pacific and Atlantic ITCZs, and nearly everywhere in the equatorial region. In the eastern tropical Pacific, the standard deviation shows a local

maximum along the equator that suggests significant ENSO-related variability. The larger standard deviation values are seen along the westerly wind band of the northern hemisphere, which is a region with large wind speed variability (e.g., Chen et al. 2003). Maximum standard deviation values are seen over the western side of the basins over the Kuroshio and Gulf Stream where the annual mean evaporation is also large (see Fig. 1, upper panel).

*b. Seasonal variability*

An exploratory EOF analysis was first applied to the weekly latent heat flux time series (not shown) and the first two EOFs captured the annual component of the seasonal cycle. The third EOF had interannual character combined with semi-annual and 4-month periodicities. To better describe the seasonal cycle we used harmonic analysis and least square fitted the first three harmonics (annual, semi-annual and 4-month) of the seasonal cycle to the time series of weekly latent heat fluxes at every grid point. The amplitude and phases of these harmonics are shown in Figs. 2 and 3, respectively.

The patterns of the amplitudes of the first three latent heat flux harmonics (Fig. 2) correspond reasonably well with the amplitudes of the first, second and fourth (3-month) harmonics of wind speed calculated by Chen et al. (2003) using six years (1993-1998) of TOPEX altimeter observations on a 1°×1° grid. In their analysis, Chen et al. (2003) used the fourth (3-month) harmonic instead of the third (4-month) as we did for latent heat flux. However, most likely their 4-month amplitude pattern is a mixture of the third and fourth harmonics dominated by the third because they used a monthly dataset. Chen et al. (2003) pointed out that the annual harmonic dominated the wind speed variability except in the Asian monsoon area (Arabian Sea, Bay of Bengal, South China Sea and the coastal waters of northwest Australia) where, although the fourth harmonic was noticeable, the strongest was the semiannual component. This holds true as well for our analysis of latent heat flux. For example, in the Arabian Sea where the monsoon is strongest, the ratio of semiannual to annual latent heat flux amplitudes estimated from Fig. 2 is about 30/20=1.5, which agrees very well with the corresponding ratio for wind speed estimated by Chen et al. (2003) to be between 1 and 2 (see their Fig. 4).

The larger amplitudes of the first latent heat flux harmonic are in the mid- and high-latitude oceans and are associated with the westerly wind bands (Fig. 2, upper panel).

The northern hemisphere shows larger amplitudes than the southern hemisphere because it contains more land, which creates stronger fluxes, particularly over the western part of the oceans. The maximum annual amplitude is found in the Kuroshio Extension (> 80 W m$^{-2}$). In the tropics, the larger annual amplitudes are off the equator and correspond to the easterly trade wind regions. The amplitudes are very small along the equator except in the Gulf of Guinea where the larger amplitudes are associated with the southeasterly winds and extend northward just beyond the equator. As noted earlier, this pattern compares well with the annual wind speed amplitudes of Chen et al. (2003) but the larger latent heat flux amplitudes in the cold tongue regions of the eastern Pacific and Atlantic are not clearly represented in the wind speed amplitudes, which indicates that annual upwelling may play a role there.

The phase of the first harmonic mainly reflects high evaporation in late fall/early winter and low evaporation in late spring/early summer in both hemispheres from 20° to 40° latitude (Fig. 3, upper panel). However, there are also significant phase differences within each hemisphere. In the northern hemisphere along the westerly wind band evaporation peaks around November-December and it leads the maximum evaporation of the northeast trades by about 90 days. In the southern hemisphere, the larger amplitudes in annual evaporation are found in the northeast and southwest part of the three basins (greater than 20 W m$^{-2}$). In the northeast regions, there is evidence of westward phase propagation in agreement with the first harmonic of sea level observed by the TOPEX altimeter and simulated with an ocean general circulation model (Fu and Smith 1996). Fu and Smith (1996) attributed the westward phase propagation in the southern Indian Ocean to Rossby waves in response to the wind forcing (see also, Perigaud and Delecluse 1993; Wang et al. 2001) and the ones in the northeastern South Pacific and South Atlantic as associated with the coastal upwelling systems off the coasts of South America and Africa between 0° and 30°S. The westward propagating sea level increase associated with these features corresponds to a thermocline deepening and upper-ocean warming, which may be responsible for the increased evaporation along their path. In the South Pacific and South Atlantic the signal starts near the eastern boundary in February-March and propagates to the interior in the following months. South of the South Pacific cold

tongue at about 20°S there is a strong phase shift but the amplitude is very small there (see Fig. 2, middle) so this may not be a significant feature.

As noted earlier, the main structure in the amplitudes of the second harmonic in latent heat flux (Fig. 2, middle) can be linked to the second harmonic of the Asian monsoon. The largest amplitudes are found in the Arabian Sea (>30 W m$^{-2}$) where it is stronger than the annual harmonic. The Asian monsoon region is out of phase with the region of moderate amplitudes in the Gulf of Alaska (Fig. 3, middle), a feature also observed in the semiannual harmonic of SST (Weare 1977) and 700 mb heights (Lanzante 1983, 1985). The semiannual harmonic also shows moderate amplitudes (Fig. 2, middle) over the California Current System, a region where semiannual variability has been observed in the upper ocean thermal structure (Mendelssohn et al. 2004). In that region, the semiannual phase (Fig. 3, middle) shows evidence of westward phase propagation between 20°N and 30°N across the North Pacific. In the equatorial Atlantic there is moderated enhanced evaporation east of 30°W during May and November, which correspond with the semiannual intensification of the southeast trades (Philander and Pacanowski 1986; Lumpkin and Garzoli 2005). In the North and South Atlantic there are nearly simultaneous enhanced evaporation at about 20° latitude during January-February and July-August with some evidence of westward phase propagation. Examination of the wind bursts and enhanced evaporation events reported by Katsaros et al. (2003) indicates that they may be associated with the second harmonic.

The main features of the amplitude pattern of the third harmonic (Fig. 2, lower) are three regions with relatively large latent heat fluxes (> 15 W m$^{-2}$) in the Arabian Sea and near the dateline in the central North and South Pacific at about 20° latitude. The region in the Arabian Sea peaks in February, June and October. The other two regions are out of phase with the one in the North Pacific peaking in March, July and November. The region in the central North Pacific extends to the northwest into the California Current System region where there is evidence of a 4-month harmonic is the upper ocean thermal structure (Mendelssohn et al. 2004).

c. El Niño variability

To describe the interannual variability of the weekly latent heat fluxes we removed the seasonal cycle at every grid point estimated as the sum of the three harmonics

described in section 2.*b*. After removing the seasonal cycle, the leading EOF of the anomalous latent heat fluxes (Fig. 4) accounts for 5% of the global anomalous variance. To evaluate the significance of the EOFs we first applied North's rule of thumb (North et al. 1982) which gives a quantitative estimate of the separation between the eigenvalues. The sampling errors of the first and second eigenvalues weakly overlap while the sampling errors of the other eigenvalues overlap strongly. This indicates that only the first EOF may be interpretable and also that the issue of significances should be looked into with more detail.

The amplitude time series and spatial correlation pattern of the first EOF (Fig. 4) appear to capture the signal that was hinted at in the standard deviation plot (Fig. 1b) and by the third EOF of the exploratory EOF analysis (not shown) and which we suspect may be associated with the 1997-1998 El Niño. To further evaluate the significance of this EOF we estimated the 95% percent critical correlation value of the space pattern using the method of Davis (1976). This value closely resembles the ±0.21 contours shown in the upper panel of Fig. 4 (except in the eastern equatorial Pacific east of about 100°W) indicating that overall the main features in the space pattern of the first EOF do appear to be significant.

A final evaluation of significance of the first EOF of latent heat flux is done by comparing its spatial structure (Fig. 4, upper) with well-know El Niño patterns in surface and tropospheric variables (e.g., Zhang et al. 1997; Garreaud and Battisti 1999; Mestas-Nuñez and Enfield 2001) and discussing its consistency with the "atmospheric bridge" concept for ENSO teleconnections (Lau and Nath 1994; Klein et al. 1999).

In the Pacific, the first EOF shows reduced evaporation in a region extending from just south of the equator near the dateline to the southeast, possibly due to weakening of the southeasterly trade winds observed during El Niño. Simultaneously, enhanced evaporation rates are observed during April 1997 – April 1998 (Fig. 4, lower) in the cold tongue region of the Pacific, where usually evaporation is low, possible due to increased SST there during El Niño. Areas of enhanced evaporation are also seen around the Maritime Continent and in the regions extending from the far western off-equatorial northern and southern tropical Pacific to the northeast and southeast, respectively. These mid-latitude areas of increased evaporation may be associated with increased subsidence

associated with the increased descending Hadley flow observed there during El Niño (Oort and Yienger 1996; Mestas-Nuñez and Enfield 2001; Wang 2002a). The enhanced evaporation over the midlatitude North Pacific is consistent with this region being a major moisture source during the 1997-1998 El Niño (Sohn et al. 2004). The reduced evaporation over the Kuroshio Extension may be related to weakened Hadley flow there during El Niño (Mestas-Nuñez and Enfield 2001; Wang 2002a)

In the Atlantic and Indian Oceans, the first EOF of interannual latent heat flux also shows significant structure which may be reconciled with the known surface and tropospheric ENSO patterns through the atmospheric bridge mechanism (Enfield and Mayer 1997; Klein et al. 1999). During the warm phase of ENSO convective activity normally in the western Pacific moves eastward to the central and eastern Pacific. This leads to an anomalous Walker circulation with regions of downward motion between Indonesia and the dateline as well as over northern South America, while the opposite holds true between the dateline and South America. In the Atlantic, the downward motion over South America is associated with weakened Hadley circulation, which leads to reduced subsidence over the midlatitude Atlantic (Mestas-Nuñez and Enfield 2001; Wang 2002b). In the southern Indian Ocean, the off-equatorial decrease in evaporation may be explained in a similar way as for the midlatitude Atlantic. However, the region of enhanced evaporation near the equator may be related to an increase of the southeasterly trade winds associated with the anomalous Walker circulation there (Mestas-Nuñez and Enfield 2001).

The first EOF pattern can also be compared to the ENSO latent heat flux pattern obtained from the leading mode of nonseasonal covariability between the latent heat flux and the greenhouse effect. Gershunov and Roca (2004) estimated this pattern using canonical correlation analysis applied to 5 years (January 1992 to December 1996) of satellite latent heat fluxes from HOAPS and greenhouse effect estimates based on observations of outgoing longwave radiation from NOAA satellites (see their Fig. 11c). The agreement between the latent heat flux ENSO pattern of Gershunov and Roca and that of our first EOF is very good, further supporting our interpretation of Fig. 4 as capturing the 1997-1998 El Niño signal.

### 3. Summary and concluding remarks

We have investigated the spatial and temporal structure of seasonal and anomaly variability of oceanic evaporation using a 3-year (1996-1998) 1° × 1° gridded dataset of weekly latent heat fluxes derived from merged satellite observations (Bentamy et al. 2003).  The main goal of this study was to see if this dataset is able to capture the strong signal of the 1997-1998 El Niño and thus support extending this satellite product further for climatic applications.

The seasonal cycle of the latent heat flux data was obtained from harmonic analysis by fitting the first three harmonics to the data.  Most of the amplitude patterns of the latent heat flux harmonics can be traced to the amplitude patterns of the seasonal harmonics of wind speed as estimated from six years (1993-1998) of TOPEX altimeter data (Chen et al. 2003). The first harmonic captures an oscillation that reflects high evaporation in late fall/early winter and low evaporation in late spring/early summer in both hemispheres. The northern hemisphere has larger amplitudes, as expected from the difference in land distribution between the hemispheres, with maximum evaporation values over the western side of the North Pacific and North Atlantic oceans. Superimposed on this large-scale oscillation, the first harmonic also shows significant phase differences within each hemisphere, which in the northeast region of the southern Indian Ocean may be associated with westward propagating Rossby waves and in the cold tongue regions of the South Pacific and South Atlantic with seasonal upwelling.

The main feature of the semiannual harmonic are its large values over the Asian monsoon region, about 1.5 times larger than the annual in the Arabian Sea, and which is out of phase with the high latitude North Pacific. Other regions of semiannual variability are the California Current System region, the equatorial Atlantic east of 30°W and the North and South Atlantic at about 20° latitude.  All of these regions show moderate semiannual variability in wind speed (Chen et al. 2003).  The third latent heat flux harmonic is composed of three regions of relatively large variability which are:  the Arabian Sea, the central North Pacific to the southeast into the California Current System region, and the central South Pacific.

When the seasonal cycle estimated from the first three harmonics is removed from the latent heat flux data, the leading EOF mode describes a signal that is only weakly

separable from the rest according to North's rule of thumb (North et al. 1982). However, we showed that the main features in its correlation pattern are statistically significant. More importantly, comparison of this EOF pattern with know surface and atmospheric patterns associated with ENSO having in mind the "atmospheric bridge" concept (Lau and Nath 1994), as well as with the leading pattern of coupled interannual variability between latent heat flux and the greenhouse effect (Gershunov and Roca 2004) support our interpretation of the leading EOF of latent heat flux as capturing the 1997-1998 El Niño signal.

The main structure of the 1997-1998 El Niño signal is enhanced tropical evaporation over the eastern tropical Pacific, around the Maritime Continent, mid-latitude North and South Pacific, and equatorial Indian Ocean but reduced evaporation elsewhere. In the Pacific, the regions of enhanced evaporation coincide with regions of large sea surface salinity (SSS) variability simulated by an oceanic general circulation model for 1990-2001 (Wang and Chao 2004). This suggests that the global El Niño evaporation pattern may induce a similar SSS anomaly pattern, a hypothesis that could be tested with the future SSS observations from space and that may help explain the break down of the strong interannual (inverse) correlation between precipitation and SSS during some (e.g. 1982-1983 and 1987) El Niño events (Delcroix 1998).

The detection of the 1997-1998 El Niño signal in our satellite evaporation estimates illustrates the potential of satellite evaporation products for climate studies. The results of this study justify extending our merged satellite latent heat flux dataset to 10 years, which will allow a better description of both the seasonal cycle and the interannual variability. It will also be worthwhile to combine these fluxes with satellite estimates of the radiative heat fluxes to obtain the net surface heat fluxes. Advantages of having a good quality multiyear net surface heat flux dataset include improving the diagnostics of global climate variability, forcing ocean general circulation models, as well as having a reference for comparisons with atmospheric reanalysis and with available output from coupled and uncoupled climate model runs.

**References**

Bentamy, A., K. B. Katsaros, W. M. Drennan, and E. B. Forde, 2002: *Daily surface wind fields produced by merged satellite data. Gas Transfer at Water Surfaces*, American Geophysical Union Monograph, 343-349 pp.

Bentamy, A., K. B. Katsaros, A. M. Mestas-Nuñez, W. M. Drennan, E. B. Forde, and H. Roquet, 2003: Satellite estimates of wind speed and latent heat flux over the global oceans. *J. Climate*, **15,** 637-656.

Carton, J. A., X. Cao, B. S. Giese, and A. M. da Silva, 1996: Decadal and interannual SST variability in the tropical Atlantic Ocean. *J. Phys. Oceanogr.*, **26,** 1165-1175.

Chang, P., L. Ji, and H. Li, 1997: A decadal climate variation in the tropical Atlantic Ocean from thermodynamic air-sea interactions. *Nature*, **385,** 516-518.

Chen, G., S. W. Bi, and J. Ma, 2003: Global structure of marine wind speed variability derived from TOPEX altimeter data. *Int. J. Remote Sens.*, **24,** 5119-5133.

Chou, S. H., E. Nelkin, J. Ardizzone, and R. M. Atlas, 2004: A comparison of latent heat fluxes over global oceans for four flux products. *J. Climate*, **17,** 3973-3989.

Chou, S. H., E. Nelkin, J. Ardizzone, R. M. Atlas, and C. L. Shie, 2003: Surface turbulent heat and momentum fluxes over global oceans based on the Goddard Satellite retrievals, version 2 (GSSTF2). *J. Climate*, **16,** 3256-3273.

Curry, J. A., A. Bentamy, M. A. Bourassa, D. Bourras, E. F. Bradley, M. Brunke, S. Castro, S. H. Chou, C. A. Clayson, W. J. Emery, L. Eymard, C. W. Fairall, M. Kubota, B. Lin, W. Perrie, R. A. Reeder, I. A. Renfrew, W. B. Rossow, J. Schulz, S. R. Smith, P. J. Webster, G. A. Wick, and X. Zeng, 2004: Seaflux. *Bull. Amer. Meteor. Soc.*, **85,** 409-424.

da Silva, A. M., C. C. Young, and S. Levitus, 1994: *Atlas of Surface Marine Data*. Vol. 4, *Anomalies of Fresh Water Fluxes*, National Oceanic and Atmospheric Administration, 308 pp.

Davis, R. E., 1976: Predictability of sea surface temperature and sea level pressure anomalies over the North Pacific Ocean. *J. Phys. Oceanogr.*, **6,** 249-266.

Delcroix, T., 1998: Observed surface oceanic and atmospheric variability in the tropical Pacific at seasonal and ENSO timescales: A tentative overview. *J. Geophys. Res.*, **103,** 18611-18633.

Enfield, D. B. and D. A. Mayer, 1997: Tropical Atlantic sea surface temperature variability and its relation to El Niño-Southern Oscillation. *J. Geophys. Res.*, **102,** 929-945.

Esbensen, S. K. and V. Kushnir, 1981: The heat budget of the global ocean: An atlas based on estimates from surface marine observations. Report 29, 27 pp.

Folland, C. K., T. N. Palmer, and D. E. Parker, 1986: Sahel rainfall and worldwide sea temperatures, 1901-1985. *Nature*, **320,** 602-607.

Fu, L.-L. and R. D. Smith, 1996: Global ocean circulation from satellite altimetry and high-resolution computer simulation. *Bull. Amer. Meteor. Soc.*, **77,** 2625-2636.

Garreaud, R. D. and D. S. Battisti, 1999: Interannual (ENSO) and interdecadal (ENSO-like) variability in the southern hemisphere tropospheric circulation. *J. Climate*, **12,** 2113-2123.

Gershunov, A. and R. Roca, 2004: Coupling of latent heat flux and the greenhouse effect by large-scale tropical/subtropical dynamics diagnosed in a set of observations and model simulations. *Climate Dyn.*, **22,** 205-222.

Hasse, L. and S. D. Smith, 1997: Local sea surface wind, wind stress, and sensible and latent heat fluxes. *J. Climate*, **10,** 2711-2724.

Josey, S. A., E. C. Kent, and P. K. Taylor, 1998: The Southampton Oceanography Centre (SOC) Ocean-Atmosphere Heat, Momentum and Freshwater Flux Atlas. Southampton Oceanography Centre Rep. 6, 30 pp.

Kalnay, E., M. Kanamitsu, R. Kistler, W. Collins, D. Deaven, L. Gandin, M. Iredell, S. Saha, G. White, J. Woollen, Y. Zhu, M. Chelliah, W. Ebisuzaki, W. Higgins, J. Janowiak, K. C. Mo, C. Ropelewski, J. Wang, Leetmaa, R. Reynolds, R. Jenne, and D. Joseph, 1996: The NCEP/NCAR 40-year Reanalysis Project. *Bull. Amer. Meteor. Soc.*, **77,** 437-471.

Katsaros, K. B., A. M. Mestas-Nuñez, A. Bentamy, and E. B. Forde, 2003: Wind Bursts and Enhanced Evaporation in the Tropical and Subtropical Atlantic Ocean. *Interhemispheric Water Exchange in the Atlantic Ocean, Elsevier Oceanographic Series, 68*, G. J. Goni and P. Malanotte-Rizzoli, Eds., Elsevier Science, 463-474.

Klein, S. A., B. J. Soden, and N. C. Lau, 1999: Remote sea surface temperature variations during ENSO: Evidence for a tropical Atmospheric bridge. *J. Climate*, **12,** 917-932.

Kubota, M., N. Iwasaka, S. Kizu, M. Konda, and K. Kutsuwada, 2002: Japanese Ocean Flux Data Sets with Use of Remote Sensing Observations (J-OFURO). *J. Oceanogr.*, **58,** 213-225.

Kubota, M., A. Kano, H. Muramatsu, and H. Tomita, 2003: Intercomparison of various surface latent heat flux fields. *J. Climate*, **16,** 670-678.

Lanzante, J. R., 1983: Some singularities and irregularities in the seasonal progression of the 700 mb height field. *J. Appl. Meteorol.*, **22,** 967-981.

——, 1985: Further studies of singularities associated with the semiannual cycle of 700 mb heights. *Mon. Wea. Rev.*, **113,** 1372-1378.

Lau, N.-C. and M. J. Nath, 1994: A modeling study of the relative roles of tropical and extratropical anomalies in the variability of the global atmosphere-ocean system. *J. Climate*, **7,** 1184-1207.

Lumpkin, R. and S. L. Garzoli, 2005: Near-surface circulation in the tropical Atlantic Ocean. *Deep-Sea Res. Pt. I*, **52,** 495-518.

McPhaden, M. J., 1999: Genesis and evolution of the 1997-98 El Niño. *Science*, **283,** 950-954.

Mendelssohn, R., F. B. Schwing, and S. J. Bograd, 2004: Nonstationary seasonality of upper ocean temperature in the California Current. *J. Geophys. Res.*, **109**.

Mestas-Nuñez, A. M. and D. B. Enfield, 2001: Eastern Equatorial Pacific SST variability: ENSO and non-ENSO components and their climatic associations. *J. Climate*, **14,** 391-402.

Moura, A. D. and J. Shukla, 1981: On the dynamics of droughts in northeast Brazil: Observations, theory and numerical experiments with a general circulation model. *J. Atmos. Sci.*, **38,** 2653-2675.

North, G. R., T. L. Bell, R. F. Cahalan, and F. J. Moeng, 1982: Sampling errors in the estimation of empirical orthogonal functions. *Mon. Wea. Rev.*, **110,** 699-706.

Oort, A. H. and J. J. Yienger, 1996: Observed interannual variability in the Hadley Circulation and its connection to ENSO. *J. Climate*, **9,** 2751-2767.

Peixoto, J. P. and A. H. Oort, 1992: *Physics of Climate*. American Institute of Physics, 520 pp.

Perigaud, C. and P. Delecluse, 1993: Interannual sea level variations in the tropical Indian Ocean from Geosat and shallow water simulations. *J. Phys. Oceanogr.*, **23,** 1916-1934.

Philander, S. G. H. and R. C. Pacanowski, 1986: A model of the seasonal cycle in the tropical Atlantic Ocean. *J. Geophys. Res.*, **91,** 14,192-14,206.

Reynolds, R. W. and T. M. Smith, 1994: Improved global sea surface temperature analysis using optimum interpolation. *J. Climate*, **7,** 929-948.

Schulz, J., J. Meywerk, S. Ewald, and P. Schlüssel, 1997: Evaluation of satellite-derived latent heat fluxes. *J. Climate*, **10,** 2782-2795.

Schulz, J., P. Schlüssel, and H. Grassl, 1993: Water vapor in the atmospheric boundary layer over oceans from SSM/I measurements. *Int. J. Remote Sens.*, **14,** 2773-2789.

Smith, S. D., 1988: Coefficients for sea surface wind stress, heat flux and wind profiles as a function of wind speed and temperature. *J. Geophys. Res.*, **93,** 15,467-15,472.

Sohn, B. J., E. A. Smith, F. R. Robertson, and S. C. Park, 2004: Derived over-ocean water vapor transports from satellite-retrieved E-P datasets. *J. Climate*, **17,** 1352-1365.

Wang, C., 2002a: Atmospheric circulation cells associated with the El Niño–Southern Oscillation. *J. Climate*, **15,** 399-419.

——, 2002b: Atlantic climate variability and its associated atmospheric circulation cells. *J. Climate*, **15,** 1516-1536.

Wang, L. P., C. J. Koblinsky, and S. Howden, 2001: Annual Rossby wave in the southern Indian Ocean: Why does it "appear" to break down in the middle ocean? *J. Phys. Oceanogr.*, **31,** 54-74.

Wang, X. and Y. Chao, 2004: Simulated sea surface salinity variability in the tropical Pacific. *Geophys. Res. Lett.*, **31,** doi:10.1029/2003GL018146.

Weare, B. C., 1977: Empirical orthogonal function analysis of Atlantic Ocean surface temperatures. *Quart. J. Roy. Meteor.  Soc.*, **103,** 467-478.

Xie, S. P. and S. G. H. Philander, 1994: A coupled ocean-atmosphere model of relevance to the ITCZ in the eastern Pacific. *Tellus A*, **46,** 340-350.

Zhang, Y., J. M. Wallace, and D. S. Battisti, 1997: ENSO-like interdecadal variability: 1900-93. *J. Climate*, **10,** 1004-1020.

**FIGURE CAPTIONS**

**Fig. 1.** Maps of the mean (upper panel) and standard deviation (lower panel) of the 3-year (1996-1998) weekly latent heat flux time series in W m$^{-2}$. The solid white (black) contours in the upper and lower panels respectively correspond to 150 (75) and 50 (35) W m$^{-2}$. The white areas are regions of missing data.

**Fig. 2.** Amplitudes of the annual (top panel), semi-annual (middle panel), and 4-month (bottom panel) harmonics of the weekly latent heat flux time series in W m$^{-2}$. The solid white (black) contours in the upper, middle and bottom panels correspond respectively to 50 (20), 30 (10), and 15 (5) W m$^{-2}$. The white areas are regions of missing data.

**Fig. 3.** Phases of the annual (top panel), semi-annual (middle panel), and 4-month (bottom panel) harmonics of the weekly latent heat flux time series. The phase values correspond closely with the day of the year when the latent heat flux reaches a maximum. For the semi-annual and 4-month harmonics one more maximum and two more maxima respectively occur 180 and 120/240 days after the day indicated. The white areas are regions of missing data.

**Fig. 4.** Leading EOF of the weekly latent heat flux anomalies describing El Niño variability and accounting for 5% of the global anomalous variance. The latent heat flux anomalies were calculated by removing from every time series the mean (Fig. 1, upper) as well as the seasonal cycle estimated by adding the three harmonics shown in Figs. 2 and 3. Upper panel: spatial distribution of the temporal correlation coefficient between the latent heat flux anomalies and the modal reconstruction over the Niño-3 index region indicated with the dashed box. The solid blue and red lines indicate the +0.21 and -0.21 contours, respectively. Lower panel: temporal reconstruction of the mode related variability averaged over the Niño-3 index region.
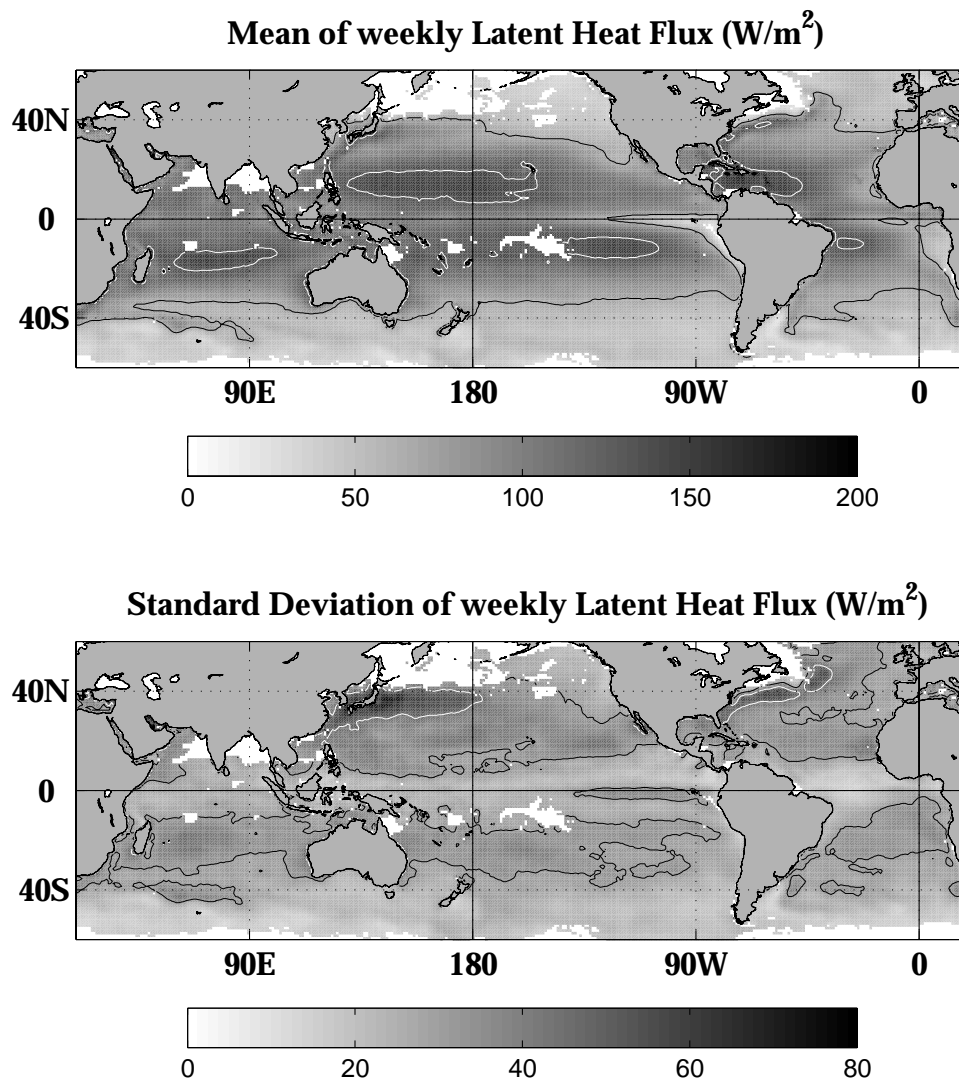
**Fig. 1.** Maps of the mean (upper panel) and standard deviation (lower panel) of the 3-year (1996-1998) weekly latent heat flux time series in W m$^{-2}$. The solid white (black) contours in the upper and lower panels respectively correspond to 150 (75) and 50 (35) W m$^{-2}$. The white areas are regions of missing data.
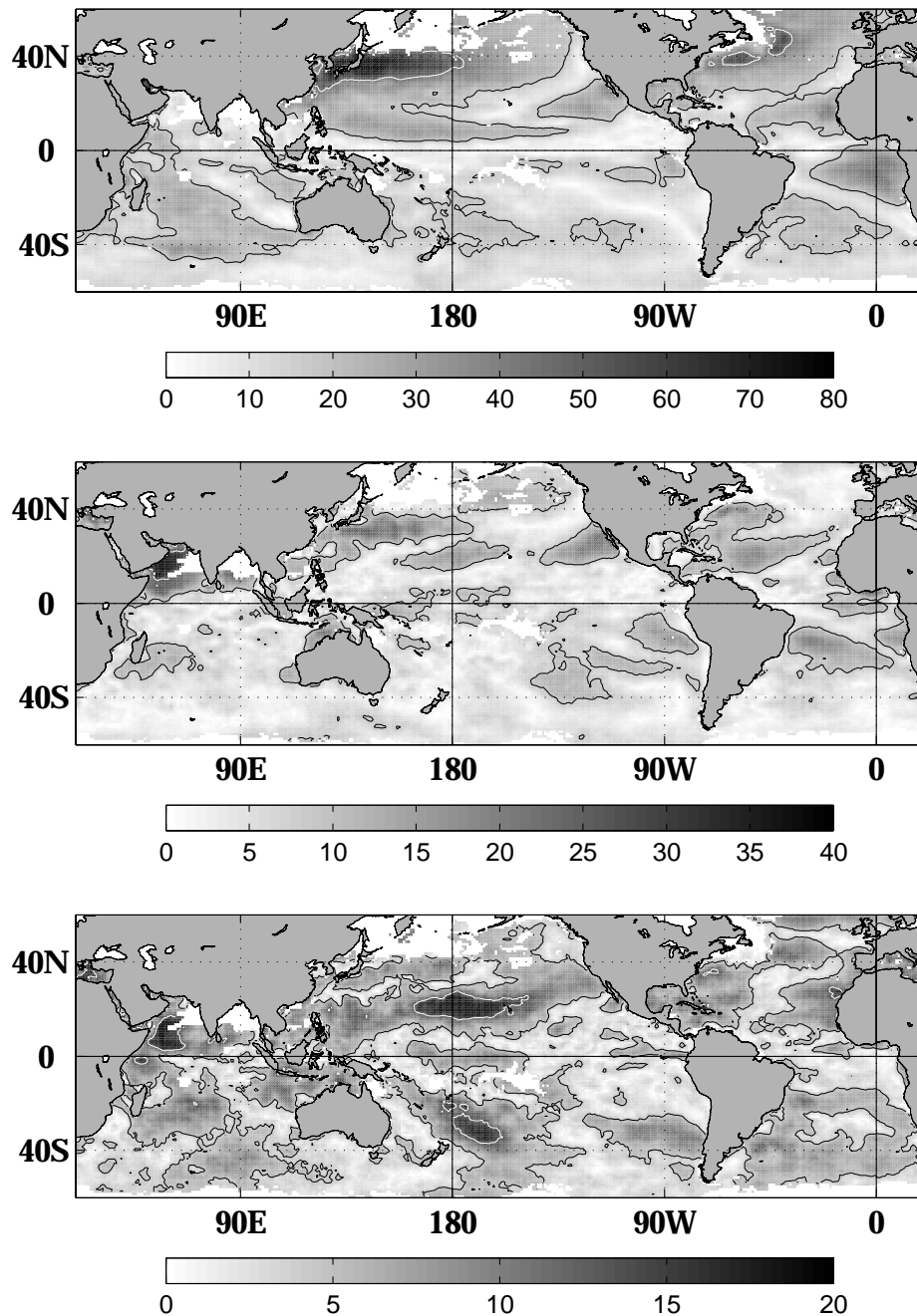
**Fig. 2.** Amplitudes of the annual (top panel), semi-annual (middle panel), and 4-month (bottom panel) harmonics of the 1996-1998 weekly latent heat flux time series in W m$^{-2}$. The solid white (black) contours in the upper, middle and bottom panels correspond respectively to 50 (20), 30 (10), and 15 (5) W m$^{-2}$. The white areas are regions of missing data.
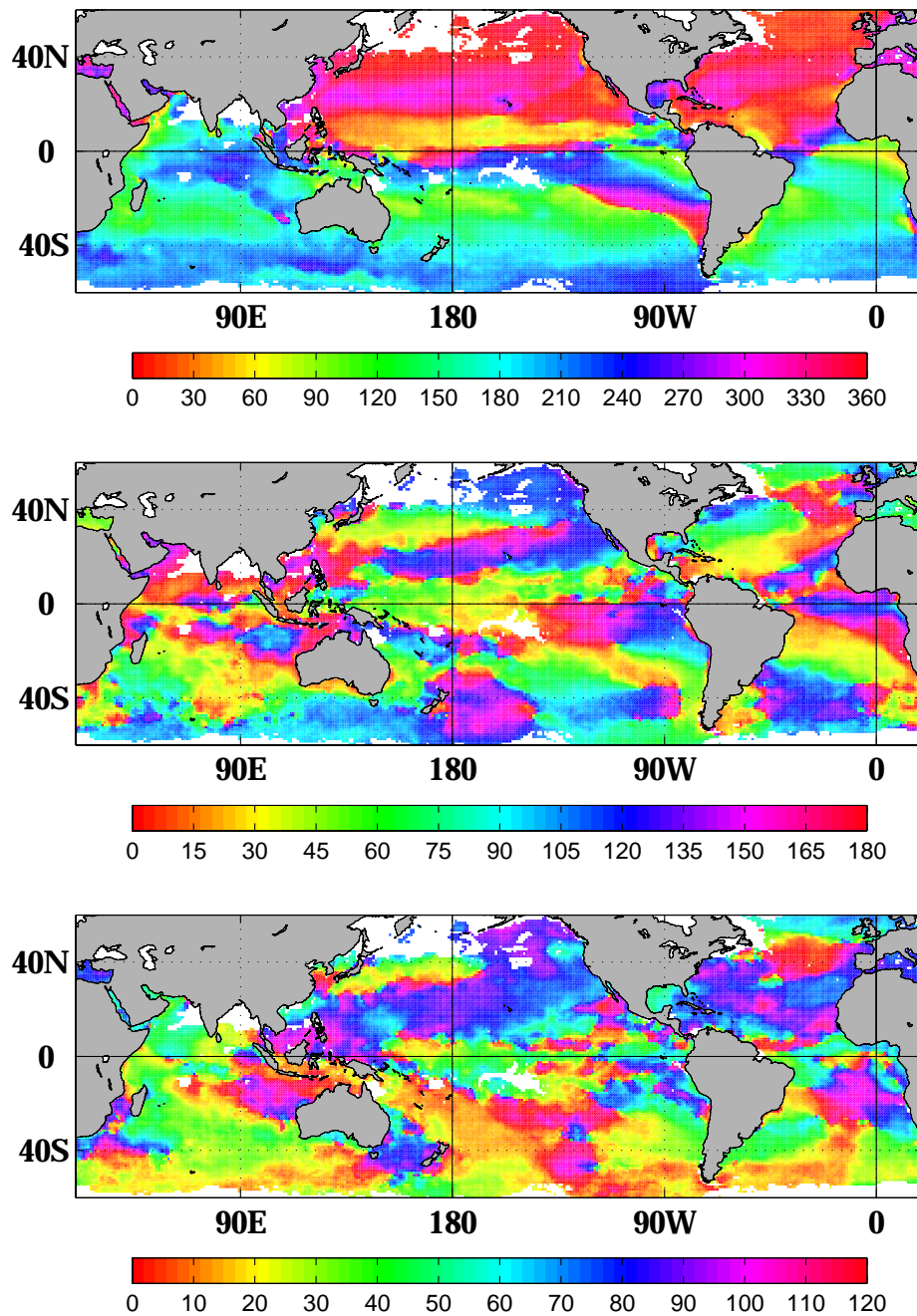
**Fig. 3.** Phases of the annual (top panel), semi-annual (middle panel), and 4-month (bottom panel) harmonics of the weekly latent heat flux time series. The phase values correspond closely with the day of the year when the latent heat flux reaches a maximum. For the semi-annual and 4-month harmonics one more maximum and two more maxima respectively occur 180 and 120/240 days after the day indicated. The white areas are regions of missing data.
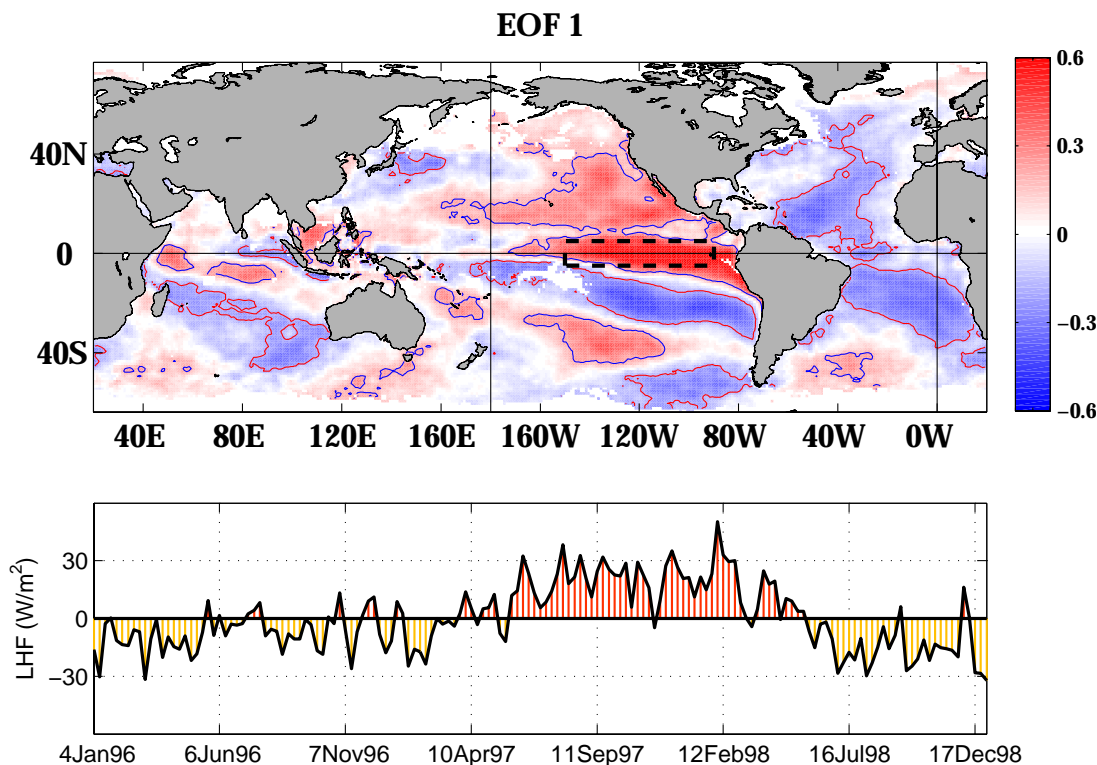
**EOF 1**



**Fig. 4.** Leading EOF of the weekly latent heat flux anomalies describing El Niño variability and accounting for 5% of the global anomalous variance. The latent heat flux anomalies were calculated by removing from every time series the mean (Fig. 1, upper) as well as the seasonal cycle estimated by adding the three harmonics shown in Figs. 2 and 3. Upper panel: spatial distribution of the temporal correlation coefficient between the latent heat flux anomalies and the modal reconstruction over the Niño-3 index region indicated with the dashed box. The solid blue and red lines indicate the +0.21 and -0.21 contours, respectively. Lower panel: temporal reconstruction of the mode related variability averaged over the Niño-3 index region.